Nanoscale Electrodes by Conducting Atomic Force Microscopy: Oxygen Reduction Kinetics at the Pt|$CsHSO_4$ Interface

Mary W. Louie,[†] Adrian Hightower,[§] and Sossina M. Haile[†,‡,]*

[†]Department of Chemical Engineering, and [‡]Department of Materials Science, California Institute of Technology, Pasadena, California 91125, and [§]Department of Physics, Occidental College, Los Angeles, California 90041

ABSTRACT We quantitatively characterized oxygen reduction kinetics at the nanoscale Pt|$CsHSO_4$ interface at ∼150 °C in humidified air using conducting atomic force microscopy (AFM) in conjunction with AC impedance spectroscopy and cyclic voltammetry. From the impedance measurements, oxygen reduction at Pt|$CsHSO_4$ was found to comprise two processes, one displaying an exponential dependence on overpotential and the other only weakly dependent on overpotential. Both interfacial processes displayed near-ideal capacitive behavior, indicating a minimal distribution in the associated relaxation time. Such a feature is taken to be characteristic of a nanoscale interface in which spatial averaging effects are absent and, furthermore, allows for the rigorous separation of multiple processes that would otherwise be convoluted in measurements using conventional macroscale electrode geometries. The complete current−voltage characteristics of the Pt|$CsHSO_4$ interface were measured at various points across the electrolyte surface and reveal a variation of the oxygen reduction kinetics with position. The overpotential-activated process, which dominates at voltages below −1 V, was interpreted as a charge-transfer reaction. Analysis of six different sets of Pt|$CsHSO_4$ experiments, within the Butler−Volmer framework, yielded exchange coefficients (α) for charge transfer ranging from 0.1 to 0.6 and exchange currents (i_0) spanning 5 orders of magnitude. The observed counter-correlation between the exchange current and exchange coefficient indicates that the extent to which the activation barrier decreases under bias (as reflected in the value of α) depends on the initial magnitude of that barrier under open circuit conditions (as reflected in the value of i_0). The clear correlation across six independent sets of measurements further indicates the suitability of conducting AFM approaches for careful and comprehensive study of electrochemical reactions at electrolyte−metal−gas boundaries.

KEYWORDS: solid acid · scanning probe microscopy · microelectrode · impedance spectroscopy · cyclic voltammetry · fuel cells · electrode kinetics

The power output of high-performance, thin-electrolyte fuel cells is, by definition, limited by the rate of electrochemical reactions at the electrode rather than by ion transport through the electrolyte. Accordingly, substantial effort has been directed toward understanding electrochemical reaction pathways and identifying rate-limiting steps, with the ultimate aim of developing new electrode materials and/or structures with enhanced activity. The vast majority of such electrochemical studies have relied on fuel cell electrodes of macroscopic dimensions, in some cases with geometrically well-defined structures[1−13] and in others with composite electrodes more directly relevant to technological applications.[14−17] While such studies have led to important insights and advances, a comprehensive understanding of reaction pathways remains elusive for virtually every fuel cell type. It is to be expected that electrochemical reactions, which occur on surfaces that naturally display nanoscale heterogeneity, themselves occur at rates that are heterogeneous on the nanometer length scale. Thus, the limitations of macroscale measurements, which, by definition, cannot probe such heterogeneity and instead provide ensemble-averaged data with little information even about the distribution range of properties, may inherently complicate elucidation of electrochemical reaction pathways. Despite the recognition that nanoscale heterogeneity may play an important role in fuel cell electrode kinetics, few studies have been directed toward explicitly uncovering variations in electrochemical reaction rates and possibly even mechanisms at the nanometer scale.

In this work, we utilize conducting atomic force microscopy (AFM) for quantitative electrochemical characterization of metal|solid electrolyte interfaces. Configurationally, the approach is similar to that employed in recent studies in which conducting AFM has been employed to evaluate nanoscale heterogeneity in the transport properties of ion conducting electrolyte materials.[18−23] The electrolyte material is contacted over its entire area to an electrochemically active counter electrode (Figure 1) and the conducting AFM probe contacted to

*Address correspondence to smhaile@caltech.edu.

Received for review January 14, 2010 and accepted April 08, 2010.

10.1021/nn100084h

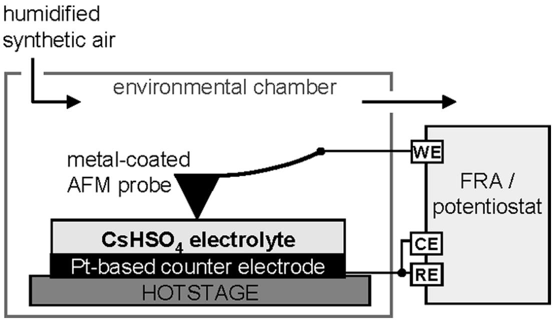

Figure 1. Schematic of nanoelectrode setup composed of an atomic force microscope coupled with an external potentiostat and a frequency response analyzer capable of measuring fA current range. The hotstage can heat samples to temperatures as high as 240 °C. The environmental chamber encloses the probe-sample assembly and is equipped with several inlet/outlet ports, enabling controlled atmospheres.

the opposite surface. Because the electrolyte is electronically blocking, net current flow through the system requires electrocatalysis to occur at sufficient rates at both the counter and working (AFM tip) electrode. For the study of the distribution of ion conducting and insulating regions, as has been done for polymers[18−22,24,25] and more recently for ceramics,[23] it is sufficient to scan the electrolyte surface and differentiate between regions of high and low current flow. From such measurements, it is also possible to characterize the nature of contact between the probe and electrolyte.[24,25] Here, we evaluate the complete current−voltage characteristics at each point of interest on the electrolyte surface to study directly the kinetics of the electrochemical reaction and its nanoscale heterogeneity.

The electrolyte material selected for study in this work is $CsHSO_4$, a so-called superprotonic solid acid, which exhibits a proton conductivity of $\sim 6 \times 10^{-3}$ S cm^{-1} at a moderate temperature of 150 °C.[26,27] We consider it a representative material for superprotonic solid acids, in general,[28] and specifically for those such as CsH_2PO_4, which have been demonstrated in fuel cells but require somewhat higher temperatures to attain comparably high proton conductivities.[29,30] The electrochemical reaction of interest (examined at 150 °C for all experiments in this study) is that of oxygen electroreduction. The relevant global reaction for a proton conducting electrolyte is given as

$$\frac{1}{2}O_2+2H^++2e^- \rightarrow H_2O \qquad (1)$$

An attractive feature of the conducting AFM geometry is the extreme asymmetry in the electrode areas. As discussed in detail elsewhere,[12] such asymmetry ensures that the overpotential (excess voltage drop relative to equilibrium) at the large counter electrode is negligible relative to that at the working (AFM tip) electrode. That is, because the current through each component of the cell is the same, the current density is orders of magnitude greater at the working electrode than it is at the counter electrode, and accordingly, the contribution of the counter electrode|electrolyte interface to the voltage drop measured across the system is negligible. Indeed, in the conducting AFM configuration, even the voltage drop across the electrolyte is negligible relative to that due to the finite kinetics at the working electrode. Thus, employing a nanoelectrode enables electrochemical studies of a single metal|electrolyte interface without the need for an external reference electrode, the placement of which has been shown to be problematic in solid electrolyte systems.[31,32] Such a measurement directly yields the potential at the working electrode, referenced to the counter electrode, which, in turn, for the measurement temperature of ~150 °C is at −1.13 V relative to $2H^+ + 2e^- \rightleftharpoons H_2$.

With this understanding, both cyclic voltammetry and AC impedance spectroscopy were used for quantitative electrochemical characterization. The former has the benefits of providing complete DC current−voltage characteristics at short time scales, before instrument drift becomes problematic, but cannot deconvolute resistance contributions resulting from multiple reaction steps. Impedance spectroscopy provides the benefits of deconvolution and, when carried out as a function of bias, can also provide complete current−voltage characteristics. The time scale of such measurements, however, is not sufficient to eliminate the possibility of a drifting probe−sample contact over the course of the experiment. The complementary information provided by these two techniques has proven to be indispensible in the present work.

RESULTS AND DISCUSSION

Cyclic Voltammetry. An initial comparison between the behavior of Au and Pt was performed to verify that contact could be made between the electrolyte surface and the AFM probe. Cyclic voltammograms for $Au|CsHSO_4$ and $Pt|CsHSO_4$ are presented in Figure 2. The observation of low currents, ~pA, is consistent with the small size of the AFM probe (tip radius ~40 nm). Noise appearing in the voltammograms, resulting from a combination of the relatively low spring constant of the probe cantilever and elevated operating temperatures, is minimal and does not mask any of the salient characteristics. The voltammogram for $Au|CsHSO_4$ is featureless and displays less than 0.1 pA current across all voltages. In contrast, the voltammogram for $Pt|CsHSO_4$ exhibits a peak at −0.34 V (onset of about −0.1 V) overlaid with an overpotential-activated rise in current at negative biases. At −1.1 V, the measured current for Pt is ~15 pA, over 2 orders of magnitude higher than that for Au. These observations are consistent with the relative activities of bulk gold and platinum and confirm contact by the probe tip.

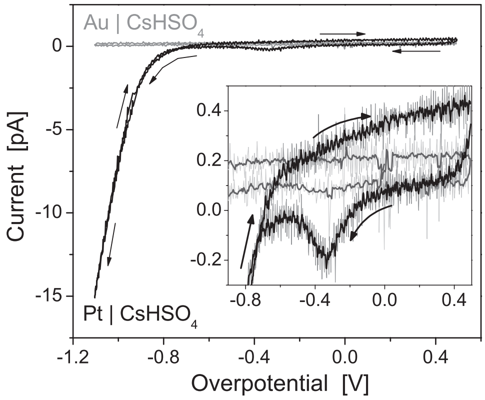

Figure 2. Comparison of typical cyclic voltammograms for Au|CsHSO$_4$ and Pt|CsHSO$_4$ collected at ~150 °C in air (~0.03 atm H_2O) with a scan rate of 100 mV s^{-1}; the voltammograms shown are those obtained after cycling to ensure stability. Inset is an enlargement of the Pt oxide reduction peak at −0.34 V and displays both raw data (gray) and smoothed data (black). The applied force was ~2 and ~0.5 μN for Au and Pt, respectively. The Pt probe utilized is identified as probe 3 in the Methods section.

The peak evident in the Pt voltammogram is readily attributed to the reduction of platinum oxide. On the basis of calculations from thermodynamic data[33] for $T = 150$ °C and $pO_2 = 0.21$ atm, reduction of PtO, PtO_2, and $Pt(OH)_2$ is expected to occur at −0.16, −0.14, and −0.06 V, respectively, whereas measured platinum oxide reduction potentials, for both smooth Pt surfaces in aqueous acidic electrolytes[34−36] and for Pt|Nafion systems,[24,37,38] range from −0.03 to −0.3 V, depending on temperature and experimental conditions. The total charge, ~0.5 pC, implied by the integrated area under the reduction peak and the scan rate, assuming the formation of any of the possible oxides, corresponds to the reduction of a plausible fraction of the Pt coating available on the AFM tip. The absence of a corresponding Pt oxidation peak on the reverse sweep indicates that chemical oxidation of Pt, which by definition, cannot generate a peak in the voltammogram, dominates the process of oxide formation over electrochemical oxidation.

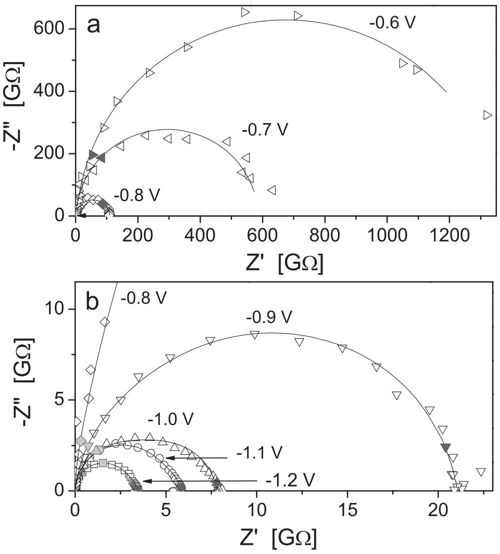

Figure 3. AC impedance spectra for Pt|CsHSO$_4$ as a function of overpotential, collected at ~150 °C in humidified air (~0.03 atm H_2O), for overpotentials between (a) −0.6 and −0.8 V, and (b) −0.8 and −1.2 V. The filled data points correspond to frequencies of 200 and 2 Hz, and solid curves indicate equivalent circuit fits to two parallel R-CPE subcircuits in series. The Pt probe utilized is identified as probe 3 in the Methods section.

While the Pt oxide reduction behavior on CsHSO$_4$ bears some similarities to that at the interface with aqueous and polymeric electrolytes, the Pt|CsHSO$_4$ system differs sharply from those in terms of interaction with hydrogen. In aqueous, acidic electrolytes or with polymer membrane electrolytes, hydrogen adsorption or desorption peaks are typically observed in the region between −0.8 and −1.2 V at temperatures between 25 and 150 °C.[24,38−43] The absence of such peaks here suggests that hydrogen sorption onto the surface of Pt is negligible in the Pt|CsHSO$_4$ system. An unfortunate consequence of this behavior is that, in contrast to aqueous and polymer systems, hydrogen adsorption peaks cannot be used to estimate the surface area of Pt available for electrocatalysis in solid acid fuel cell electrodes. Similarly, without further information on the characteristics of Pt oxide reduction, the corresponding peak in the voltammogram cannot be employed for determining the Pt|CsHSO$_4$ contact area.

Impedance Spectroscopy. Selected impedance spectra representative of oxygen reduction at the Pt|CsHSO$_4$ interface are presented as Nyquist plots in Figures 3 and 4. While the bulk of the experimental details regarding acquisition of such spectra are provided in the Methods section, some aspects are highlighted here because the high impedance of the Pt|CsHSO$_4$ system in the nanoprobe geometry requires special consideration with respect to effects from external noise. All spectra collected were corrected with an open circuit measurement which accounted for stray capacitance and other spurious contributions, and furthermore, the impedance analyzer was calibrated with precision circuits composed of high-resistance (0.01−100 GΩ) and

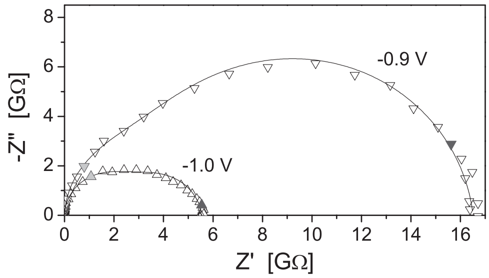

Figure 4. Typical impedance spectra for Pt|CsHSO$_4$ at overpotentials of −1.0 and −0.9 V, collected at ~150 °C in humidified air (~0.03 atm H_2O), showing the presence of two processes. The filled data points correspond to frequencies of 200 and 2 Hz, and solid curves indicate equivalent circuit fits to two parallel R-CPE subcircuits in series. The Pt probe utilized is identified as probe 2 in the Methods section.

low-capacitance (1−10 pF) elements comparable in value to those measured in the present nanoprobe system. We also verified that the impedance response is stable, that is, the spectra features are not transient artifacts, by examining the agreement between two spectra collected consecutively at −1.0 V, with one measured by sweeping the frequency in the opposite direction of the other (see Methods for details). With these precautions taken, the general features of the experimental data were found to be satisfactorily reproducible.

The Nyquist plots presented in Figures 3 and 4 reflect data collected from two different Pt probes, where the response for each was examined as a function of the applied voltage. In both cases, the total polarization resistance is a strong function of bias, spanning almost 3 orders of magnitude in Figure 3, from ~3 GΩ at −1.2 V to ~1 TΩ at −0.6 V. Proton conduction through bulk $CsHSO_4$, typically manifested in bulk conductivity measurements as an ohmic offset at high frequencies,[30] is not visible in Figures 3 and 4 because its contribution is negligible compared to the electrode processes.

In the absence of a physical model, impedance spectra are commonly analyzed by employing equivalent circuits, for which the simplest building block is a resistor (R) in parallel with a constant phase element (CPE). The latter generally represents capacitive effects and has impedance

$$Z_{\mathrm{CPE}} = \frac{1}{Q_0(i\omega)^n} \qquad (2)$$

where Q_0 is a constant, ω is the angular frequency, and n ranges from 0 to 1. When $n = 1$, the CPE element becomes a perfect capacitor with capacitance Q_0, and the parallel R-CPE subcircuit is represented in the Nyquist plot as a semicircle with its center lying on the real axes. Deviations of n from 1 are typically interpreted in terms of a distribution of relaxation times within a globally measured response.[44,45]

The impedance spectra shown in Figure 3 consist of two arcs; the frequency overlap of the two processes varied with experiment and spatial position, with some measurements more clearly depicting the presence of two electrode processes (Figure 4). The impedance spectra were fitted to an empirical equivalent circuit model composed of two parallel R-CPE circuits in series. Fitting results yielded $n > 0.9$ for both processes, indicating ideal capacitive behavior with a low dispersion in the characteristic frequency of each process. These n values are considerably higher than those observed for macroscale interfacial processes for which depression of the electrode arc in the Nyquist plot reflects n values in the range of 0.6−0.8.[4,9,12,15,16] Low n values for interfacial processes are commonly attributed to spatial heterogeneities at the electrode|electrolyte interface.[44,45] The observation of a low dispersion of relaxation times in the present measurement suggests that, at the nanoscale, averaging effects are eliminated. In turn, because of the low dispersion, it is possible from these measurements to clearly observe two processes, despite the similarity of their relaxation times. In a macroscopic measurement with low n, deconvolution of interfacial processes that are close in characteristic frequencies would likely not be possible.

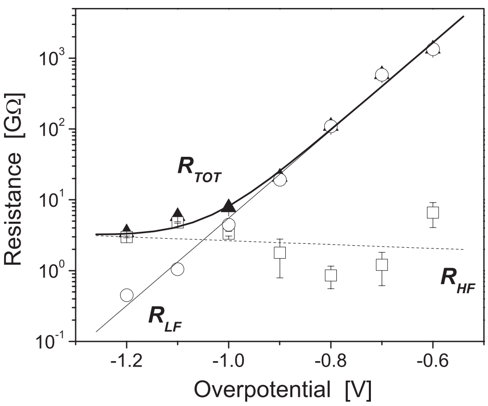

Figure 5. Total polarization resistance (R_{TOT}) and electrode resistances (R_{LF}, R_{HF}) determined by fitting AC impedance spectra (shown in Figure 3) to two parallel R-CPE circuits in series. Lines indicate the general trends of each parameter and were obtained by linear fits of R_{HF} and R_{LF} and their sum, R_{TOT}. Resistance is plotted on a logarithmic scale.

The bias dependence of the resistances associated with the two processes (Figure 5) reveals that the resistance of the low-frequency process, R_{LF}, is strongly dependent on voltage, decreasing from 1 TΩ at −0.6 V to less than 1 GΩ at −1.2 V. In the semilog plot, an apparent exponential dependence is evident. In contrast, the resistance of the high-frequency process, R_{HF}, is largely independent of bias, displaying an erratic voltage dependence between 1 and 10 GΩ that is almost within the noise of the measurement. The total electrochemical resistance, R_{TOT}, which is simply the sum of R_{LF} and R_{HF}, is accordingly dominated by R_{LF} at low bias and by the fixed value of R_{HF} at high bias. While the data here are presented for one representative set of impedance spectra, such behavior was observed in multiple measurements. An analysis of the capacitances associated with the two processes and their bias dependence is not presented here due to their relatively high fitting errors.

The electrochemical reaction of interest (eq 1) is represented by the cathodic branch of the cyclic voltammogram. Cyclic voltammograms obtained at slow scan rates (such that capacitive and other transient effects are reduced) can be employed for quantitative analysis of oxygen reduction kinetics. For such an analysis, it is essential to recognize that the oxygen reduction reaction occurs on Pt metal only at voltages negative of that for the Pt−PtO_x couple; at all other voltages, $O_2 + 4H^+ + 4e^- \rightleftharpoons 2H_2O$ occurs on platinum *oxide*. An implication of Pt oxide formation is that, for a fuel

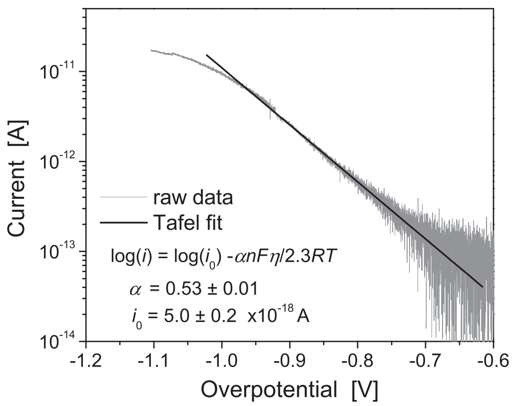

Figure 6. Semilog plot of the cathodic branch of the cyclic voltammogram for Pt|CsHSO$_4$. The voltammogram was collected with a 5 mV s^{-1} scan rate at ~150 °C in humidified air (~0.03 atm H$_2$O). The exchange coefficient and exchange current can be extracted from the slope and intercept, respectively, by fitting the linear regime to the Tafel equation (eq 6). The Pt probe utilized is identified as probe 3 in the Methods section.

cell under open circuit conditions, platinum catalyst at the cathode is oxidized, and the initial current drawn contains a contribution from Pt oxide reduction.

Analysis of Oxygen Reduction Kinetics. The behavior revealed in Figure 5 suggests that the DC current across the Pt|CsHSO$_4$ interface should, like the AC resistance, display an exponential dependence on bias within an appropriate range of voltages. In Figure 6, we plot, on a semilog scale, data obtained from the return sweep (implying the oxide has already been reduced to the metal) of the cathodic branch of a cyclic voltammogram collected at a 5 mV s^{-1} scan rate, and indeed, linearity is observed between −1 and −0.6 V. At higher biases (beyond −1 V), the deviation from linearity in the semilog plot is readily attributed to the increasing importance of the bias-independent resistance term (Figure 5). At smaller biases (less than −0.6 V), the scatter is a result of the overall low current and a nonzero offset current (correction procedures for which are described in the Methods section). In principle, the results of Figures 5 and 6 can be numerically converted from one form to the other; however, the thermal drift in the system (estimated to be ~0.1 nm s^{-1} at 150 °C) precludes quantitative comparisons. Nevertheless, the overall agreement between the AC and DC measurements, in terms of the functional form of the data, demonstrates the robustness of the experimental approach pursued here for examining electrode kinetics. Both measurements methods are utilized, as AC impedance spectroscopy provides invaluable mechanistic information, that is, the elucidation of multiple processes and their relative time scales, whereas cyclic voltammetry enables quantification of selected kinetic parameters.

A voltage-dependent resistance is a typical feature of charge-transfer electrochemical reactions, and the exponential dependence of R_{LF} on bias suggests analysis in terms of conventional Butler−Volmer reaction kinetics. In a generic sense, the charge-transfer reaction associated with oxygen electroreduction at the Pt|CsHSO$_4$ interface can be described as[39]

$$\mathrm{O} + \mathrm{e}^- \underset{k_a}{\overset{k_c}{\rightleftharpoons}} \mathrm{R} \qquad (3)$$

where k_c and k_a are the rate constants for the cathodic and anodic directions, respectively, and a single-electron process has been assumed. The kinetics associated with this reaction can be expressed in terms of the Butler−Volmer equation

$$\frac{i}{i_0} = \exp\left[-\frac{\alpha F}{RT}\eta\right] - \exp\left[\frac{(1-\alpha)F}{RT}\eta\right] \qquad (4)$$

where i_0 is the exchange current, $\eta = E - E_{eq}$ is the overpotential, α is the exchange coefficient which ranges from 0 to 1, and F, R, and T have their usual meanings. At the large negative overpotentials selected for the analysis performed here (due to both Pt oxidation and significant offset current at small overpotentials), only the cathodic branch of the Butler−Volmer equation need be considered. For $\eta \ll 0$, eq 4 reduces to

$$i = i_0\exp\left(-\frac{\alpha F}{RT}\eta\right) \qquad (5)$$

or, in Tafel form

$$\log(i) = \log(i_0) - \frac{\alpha F}{2.3RT}\eta \qquad (6)$$

Thus, from a linear fit to the semilog data, one obtains the exchange current density (from the extrapolated intercept at zero bias or overpotential) and the exchange coefficient (from the slope). As an alternative to eq 6, one can consider introduction of a term that accounts for the observation of an additional, bias-independent process (effectively accounting for R_{HF}). Attempts to fit an appropriately modified expression, however, were largely unsuccessful because of the insensitivity of the fit parameters, and hence the determination of properties associated with the high-frequency process from the voltammograms was not pursued.

For the specific data set presented in Figure 6 and a fit over the potential range from −0.65 to −1.0 V, we obtain $\alpha = 0.53 \pm 0.01$ and $i_0 = (5.0 \pm 0.2) \times 10^{-18}$ A. Because the area of electrochemical activity at the probe tip is unknown, the value determined for the exchange current cannot be readily interpreted quantitatively or compared to literature measurements. The exchange coefficient, in contrast, is independent of these uncertainties, and its absolute value has significance. This parameter provides a measure of the asymmetry of the activation barrier for the charge transfer. For a single-electron process, α should lie between 0 and 1, with $\alpha = 0.5$ corresponding to perfect symmetry of the anodic and cathodic directions of the charge transfer step. A value of 0.53 as obtained

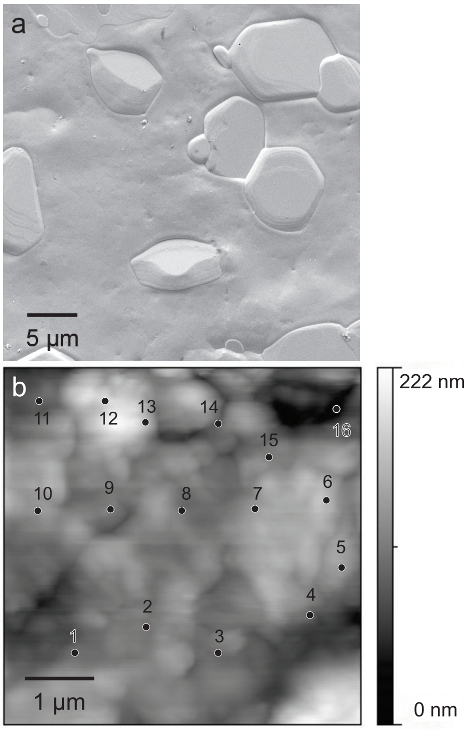

Figure 7. (a) Scanning electron micrograph of a typical $CsHSO_4$ surface acquired after electrochemical testing. (b) Topography scan of the polycrystalline $CsHSO_4$ surface collected at ~150 °C in humidified air (~0.03 atm H_2O). Labels denote nominal positions at which electrochemical measurements were acquired (Figure 8).

here falls within the range typically observed in aqueous electrolyte systems ($\alpha = 0.3-0.7$).[39]

Heterogeneity of Electrochemical Kinetics. As already noted, conducting atomic force microscopy enables an exploration of the spatial variation of electrode kinetics at Pt|$CsHSO_4$ with relative ease. A scanning electron micrograph (Figure 7a) shows typical surface features of polycrystalline $CsHSO_4$ after testing. Alongside it is an AFM topography scan of a $5 \times 5\ \mu m^2$ region, collected under operating conditions, that includes (nominal) spatial positions at which electrochemical measurements were acquired (Figure 7b). The electron micrograph shows large crystalline grains, 5−10 µm in size, whereas the topography scan, collected at higher resolution, reveals finer features (<1 µm) and a rms roughness of ~30 nm. Cyclic voltammograms measured at each position were stable upon cycling and, within a moderate range (see Methods section), insensitive to the value of the applied force, and therefore, the data are considered reliable for evaluating the electrochemical response at each position. However, the extent of thermal drift after measuring several positions precludes a precise correlation of electrochemical reaction rates with surface features.

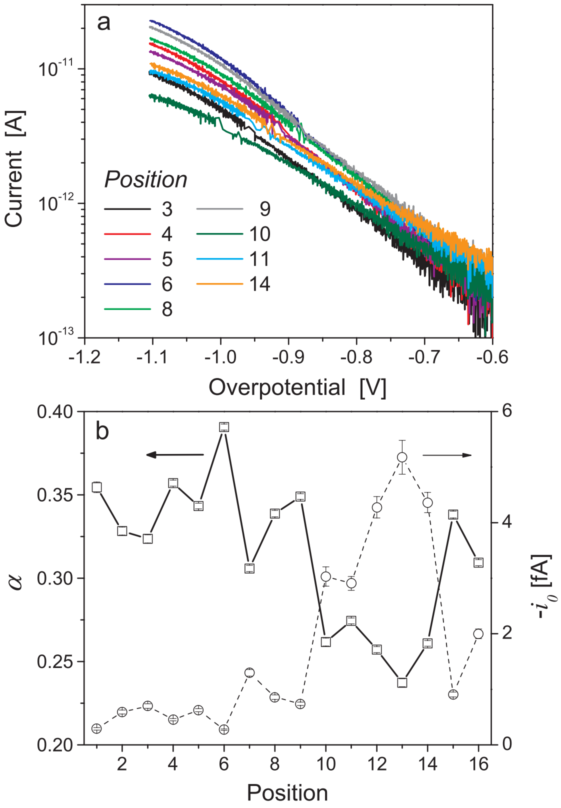

Figure 8. (a) Semilog plot of cyclic voltammograms (cathodic branch) for Pt|$CsHSO_4$ at select points across the surface shown in Figure 7b. Data were acquired with a 25 mV s^{-1} scan rate at ~150 °C in humidified air with ~0.03 atm H_2O (using probe 1, as described in the Methods section). (b) Exchange coefficient, α, and exchange current, i_0, plotted as functions of position. Parameters were extracted from fitting the linear regime of each curve in (a) to the Tafel equation (eq 6). In some instances, the error bars for α are smaller than the data markers.

The voltammograms obtained at 16 different points across the electrolyte surface (Figure 8a) exhibited features similar to that in Figure 6. Specifically, for each voltammogram, a plot of log(i) as function of bias revealed a linear regime at low bias followed by a decrease in the slope at high bias. Furthermore, impedance spectra collected at −1.0 and −0.9 V for select positions (not shown) were qualitatively similar to one another and to the results in Figure 4, indicating, in all cases, a high-frequency process with a (largely) bias-independent resistance and a low-frequency process with a resistance that decreased sharply with bias. Thus, one can conclude that the mechanistic steps involved in oxygen electroreduction at the Pt|$CsHSO_4$ interface are maintained across the electrolyte surface.

While the general shape of the voltammograms and impedance spectra were reproduced at different locations, the specific values differed substantially. For example, in the voltammetry experiments, at −0.95 V, the measured current ranged between −1.5 and −4.5 pA, a 3-fold variation. This variation is, in turn, manifested as notable variations of the exchange coefficient and exchange current across the electrolyte surface, as extracted from a Tafel analysis of the linear regime of each voltammogram, typically occurring at overpotentials between −1.0 and −0.6 V. For the specific surface shown in Figure 7b, α ranges from 0.22 to 0.39 and i_0 from 0.2 to 6 fA (Figure 8b), with the two parameters apparently counter-correlated (*i.e.*, i_0 decreases as α increases). Rather remarkably, a summary of the data for measurements of six different Pt|CsHSO$_4$ interfaces (Figure 9) reveals a counter-correlation between α and i_0 that extends over several orders of magnitude in i_0 and a factor of 6 in α. Specifically, across the six experiments, α spans from 0.1 to 0.6, with an average value of 0.3 ± 0.1, and i_0 correspondingly spans from 5×10^{-14} to 5×10^{-19} A. The spatially averaged exchange coefficient of 0.3 falls in the range, 0.35 ± 0.05, measured for the Pt wire|CsH$_2$PO$_4$ system at ~240 °C in humidified O$_2$ with ~0.35 atm H$_2$O (unpublished data). For Pt wire|CsH$_2$PO$_4$, the working electrode was a 250 μm diameter Pt wire embedded in CsH$_2$PO$_4$, and thus, the exchange coefficient from such a geometry can be treated as representative of an area-averaged electrochemical response.

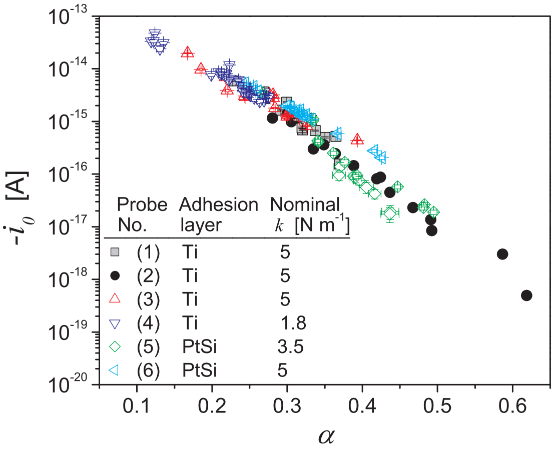

Figure 9. Semilog plot of i_0 as a function of α, showing a linear relationship across six different data sets, with the probe type indicated in the legend. Data were collected at ~150 °C in humidified air (0.01−0.03 atm H$_2$O). In some instances, the error bars for i_0 and α are smaller than the data markers.

Ignoring for the moment the counter-correlation between α and i_0, the simple observation that these parameters vary so substantially with position demonstrates that electrochemical reaction rates at Pt|CsHSO$_4$ are indeed highly influenced by nanoscale surface features of the polycrystalline electrolyte. Because variations in applied force produced no detectable change in the features of the voltammograms (see Figure 13a), changes in the extent of electrochemical reaction area are unlikely to be responsible for the large variations in i_0 or α. The relevant surface features may include the crystallographic orientation of the surface termination and the occurrence of grain or domain boundaries, or even dislocations with surface termination. Any of these features may influence the residual surface charge and be a means of influencing electrochemical reaction rates. As stated at the outset, because the electrochemical reactions in solid electrolyte fuel cells involve surface reaction steps, nanoscale heterogeneity is to be expected. The clear counter-correlation between α and i_0, however, is unexpected. The observation of a common correlation between α and i_0 for six different Pt|CsHSO$_4$ interfaces, furthermore, leaves little doubt that the phenomenon is real and suggests a common mechanism for these different interfaces. Within the Butler−Volmer framework, a large value of i_0 corresponds to a small reaction barrier between oxidized and reduced states (eq 3) under equilibrium conditions. A small value of α, which occurs for those reactions sites with large i_0, corresponds to a minimal decrease in the activation barrier under bias. The counter-correlation thus reflects a physical situation in which reaction pathways with small barriers under equilibrium conditions are relatively unaffected by the applied bias, whereas those with high barriers under equilibrium conditions are strongly decreased under bias. While there is no fundamental basis for expecting such a result, *a priori*, the counter-correlation creates a situation in which, under a given bias, all reaction sites attain a comparable level of electrochemical activity, as reflected in the value of the current (under bias) rather than the exchange current (under zero bias). A direct correlation between α and i_0, in contrast, would imply that sites with low barriers under open circuit conditions become even more active relative to other sites, under bias, and hence an immediate divergence in activity. An extensive search of the relevant literature did not uncover any studies showing such a wide-ranging, systematic and correlated variation of α and i_0 within a given electrochemical system, although, in some instances, variations as a function of a third parameter (*e.g.*, temperature, electrode/electrolyte composition, or electrode particle size)[46−53] have been explored. Further study to explicitly identify the surface features that influence electrochemical reaction kinetics at the Pt|CsHSO$_4$ interface and electrolyte−metal−gas boundaries in general is underway.

CONCLUSION

We demonstrate the use of conducting atomic force microscopy as a tool to quantitatively probe oxygen reduction kinetics in controlled environments and at elevated temperatures. We employ AC impedance spectroscopy to gain insight into the mechanism of electrocatalysis and cyclic voltammograms for quantitative analysis of oxygen reduction kinetics in the Pt|CsHSO$_4$ system. The oxygen reduction reaction is limited primarily by an overpotential-activated process that exists at low frequencies, with an additional impedance contribution, at high overpotentials, from a process that is weakly overpotential-dependent. Our ability to deconvolute these two processes derives, we believe, from the nanoscale measurements. At this scale, the measurements are free of averaging effects, leading to near-ideal capacitive behavior and minimal dispersion in the frequency response. The overpotential-activated step was interpreted as charge transfer and evaluated using the Butler−Volmer equation. Within the Butler−Volmer framework, a spatial variation in kinetics, represented by the exchange coefficient and exchange current, was observed across six independent measurements. That the correlation between log(i_0) and α for all six experiments collapses into a single line demonstrates the robustness of our experimental approach.

METHODS

Half-Cell Fabrication. $CsHSO_4$ powder was synthesized by rapid precipitation of a mixture of aqueous Cs_2SO_4 (99.99%, Alfa Aesar) and aqueous H_2SO_4 (95 wt % in water, EMD Chemicals) by acetone, followed by filtration and drying at ∼100 °C. Electrocatalyst mixtures were made from a toluene slurry composed of Pt black (>99.9%, fuel cell grade, Sigma Aldrich), Pt/C (40% on carbon black, Alfa Aesar), and $CsHSO_4$ in a Pt:Pt/C:$CsHSO_4$ weight ratio of 3:1:3; the slurry was sonicated and dried at ∼100 °C. Half-membrane electrode assemblies were fabricated by uniaxially pressing $CsHSO_4$ powder onto a Pt:Pt/C:$CsHSO_4$ composite electrode supported on Toray paper (TGP-H-120) for 20 min at 490 MPa. The $CsHSO_4$ surface of the resulting half-cell was then polished with a ∼2 μm grit silicon carbide cloth and blown with a dry air jet. Fabricated assemblies were 9.3 mm in diameter and 0.5−1 mm thick.

Experimental Conditions. Fabricated half-cells were mounted onto the hotstage of a PicoSPM atomic force microscope (Series 4500, Agilent Technologies) equipped with an environmental chamber and a scanner head with *x*−*y* and *z* ranges of ∼30 and ∼6 μm, respectively. The temperature of the hotstage was set to ∼170 °C to attain a $CsHSO_4$ surface temperature of ∼150 °C. (The temperature gradient across the cell generated an open circuit voltage of less than 1 mV.) Humidified synthetic air, generated by bubbling ∼15 sccm of air through water at room temperature (∼0.02−0.03 atm H_2O), was continuously fed through the environmental chamber. Electrochemical characterization was carried out using an externally connected potentiostat equipped with a femtoammeter and a frequency response analyzer (Modulab, Solartron Analytical), which were calibrated using high impedance circuits comprising 0.01−100 GΩ resistors and 1−10 pF capacitors. Electrochemical characterization was carried out in potentiostatic mode; voltages are applied across the entire cell (probe|$CsHSO_4$|composite electrode), with the probe as the working electrode and the large composite electrode serving as the counter and reference electrode. All voltages reported in this work are, therefore, with respect to the large composite counter electrode, that is, an air electrode reference which is −1.13 V relative to $2H^+ + 2e^- \rightleftharpoons H_2$ at ∼150 °C. To reduce contributions of external noise, the microscope was placed in a copper mesh Faraday cage which, like the shielding for the electrical leads, was grounded though the potentiostat ground. The microscope body, which was separately grounded, was electrically isolated from the cage. Stray capacitance and other spurious contributions were found to depend on the current range of the potentiostat, and therefore, open circuit corrections were obtained by withdrawing the probe from the sample and taking impedance measurements at each current range. Point-wise open circuit corrections were applied to all impedance spectra presented; a representative open circuit correction is shown in Figure 10. Short circuit measurements, obtained by contacting the conductive probe to a piece of gold foil, displayed the behavior of a pure resistor with a resistance on the order of 5 kΩ, negligible relative to the high impedances of the nanoprobe setup employed in this work.

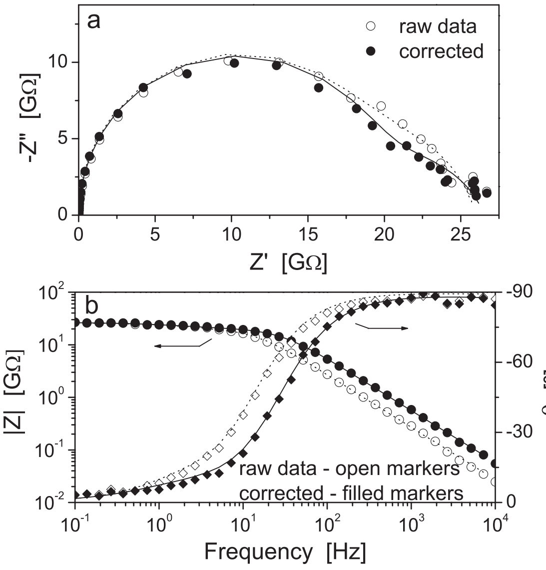

Figure 10. Representative (a) Nyquist and (b) Bode−Bode plots collected at −1.1 V before and after applying a point-wise open circuit correction. Data presented here are obtained using probe 6, as identified in Table 1.

Measurement Conditions. Cyclic voltammograms were collected by sweeping between −1.1 and 0.5 V with scan rates, ν, of 5−400 mV s^{-1}. Impedance measurements were carried out with a 100 mV perturbation about voltages ranging from −0.6 to −1.2 V with frequencies of 10^6−10^{-1} Hz. The acquisition time for each spectrum was ∼2.5 min, and three spectra for each voltage were acquired. The working electrodes were metal-coated Si-based AFM probes (MikroMasch) with specifications shown in Table 1. A majority of the platinum data presented in this work are from probes 1 and 3. Forces applied with the Pt probes were between 0.2 and 0.5 μN during electrochemical measurements and ∼0.1 μN when rastering the surface for imaging. Stationary cyclic voltammograms collected as a function of position were composed of three cycles at 100 mV s^{-1} (to attain stable voltammograms) followed by two cycles at 25 mV s^{-1} (used for quantitative analysis) for probes 1−4, and five cycles at 100 mV s^{-1} for probes 5 and 6. Impedance spectra at −1.0 and −0.9 V were measured at select spatial positions to verify that the primary features of the spectra had not changed. The thermal drift of ∼0.1 nm s^{-1}, estimated by the imaging and tracking of surface features, impacts bias-dependent impedance measurements which required ∼50 min acquisition time. On the other hand, cyclic voltammetry measurements required only several minutes of acquisition time (depending on the scan rate employed), and moreover, the voltage range used for analysis only required ∼30 s (corresponding to a drift of no more than 3 nm) to acquire.

Data Analysis. Fitting of impedance spectra was carried out using the commercial package Zview (Version 2.9b, Scribner Associates, Inc.). Spectra were fitted using two parallel R-CPE subcir-

TABLE 1. Conducting AFM Probes Employed in This Study

	adhesion layer	spring constant *k* [N m^{-1}][a]	total tip radius r_{tip} [nm][a]
probe 1	10 nm Pt on 20 nm Ti	5	40
probe 2	10 nm Pt on 20 nm Ti	5	40
probe 3	10 nm Pt on 20 nm Ti	5	40
probe 4	10 nm Pt on 20 nm Ti	1.8	40
probe 5	25 nm Pt on 5 nm PtSi	3.5	40
probe 6	25 nm Pt on 5 nm PtSi	5	40
probe 7	20 nm Au on 20 nm Cr	40	50

[a] Nominal values.

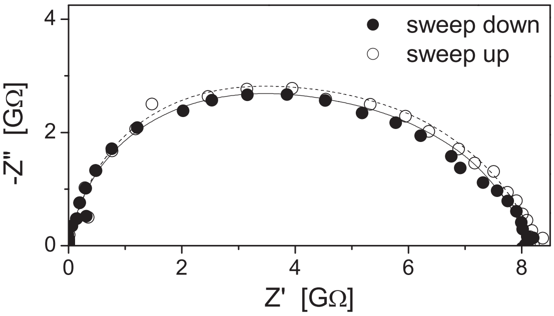

Figure 11. Two impedance spectra collected consecutively at an applied bias of −1.0 V (using probe 3, as indicated in Table 1), with the second measured by sweeping the frequency in the opposite direction of the first. The agreement between the two spectra confirms that the shape of the spectra is not a transient artifact. Spectra were acquired at ∼150 °C in air (∼0.03 atm H_2O).

cuits in series. The value of *n* for the high-frequency arc, when treated as a free parameter during fitting, exceeded unity (by no more than 10%) and was therefore held fixed at 1. Such a fitting procedure yielded *n* values of 0.91−0.98 for the low-frequency process. We verified that the appearance of two arcs in the impedance spectra was not due to transient effects; Figure 11 shows that two spectra collected consecutively, with frequencies swept in opposite directions, yield identical impedance responses.

Raw cyclic voltammetry data were corrected for nonzero offset current by fitting to a Butler−Volmer expression (eq 5) with an added constant which typically amounted to 10^{-13} A. A consequence of such a correction is the increased scatter that appears at low overpotentials in the Tafel plots (Figures 6 and 8a). For quantitative analysis of oxygen reduction kinetics, capacitive (transient) effects must be minimized, and thus, voltammograms collected at low scan rates are ideal. We verified that a scan rate of 25 mV s^{-1}, and even 100 mV s^{-1}, employed for acquiring cyclic voltammograms for spatial variation studies does not significantly affect the extracted value of α, implying a negligible impact on the conclusions drawn from data presented here. Figure 12a is a plot of cyclic voltammograms as a function of scan rate, while Figure 12b shows α values extracted from fitting of the DC data to eq 6 (for the linear regime of the Tafel plot, between −0.95 and −0.6 V). Extracted α values range from 0.35 at 400 mV s^{-1} to 0.40 at 5 mV s^{-1}; the deviation in α for the data collected at 25 mV s^{-1} from that at 5 mV s^{-1}, ±0.01, is well within the variation observed spatially (±0.1 across six different Pt|$CsHSO_4$ systems).

We confirmed that any variations in the force applied between the Pt probe and the $CsHSO_4$ surface, determined periodically using force curves, have little effect on the features of the cyclic voltammograms. Figure 13a is a series of voltammograms collected at a range of forces that is well beyond any force fluctuations observed during electrochemical measurements. Variations in both the oxygen reduction and Pt oxide reduction currents are negligible when the force is doubled, indicating a minimal effect of force on the data presented and, in particular, on the observed spatial variation of electrode kinetics. The agreement between the voltammograms, furthermore, implies that the high-frequency process, which is dominant at high bias, is not a result of contact resistance at the Pt|$CsHSO_4$ interface. We also verified that the process of lifting the probe from and reapproaching the $CsHSO_4$ surface (a procedure required for acquiring electrochemical data at various spatial positions) has a negligible impact on the features of the cyclic voltammogram (Figure 13b).

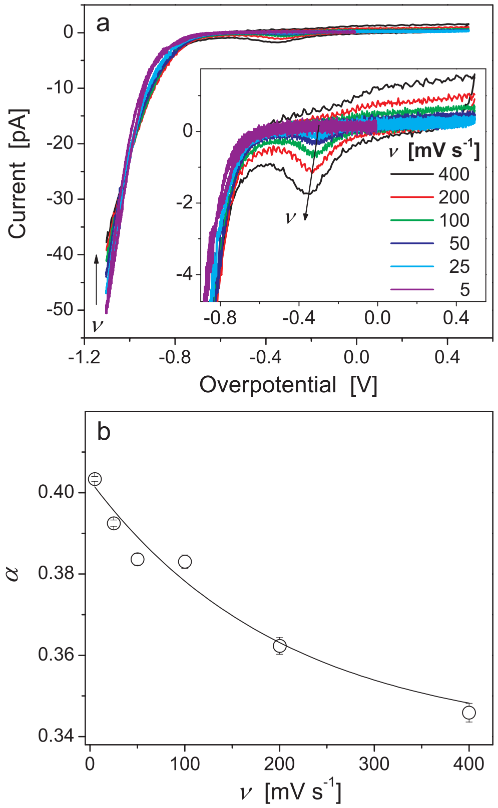

Figure 12. (a) Cyclic voltammograms for Pt|$CsHSO_4$ collected at scan rates ranging from 400 to 5 mV s^{-1} (using probe 3 listed in Table 1), and (b) corresponding exchange coefficients, α, extracted from fitting the return sweep of the cathodic branch (plotted in Tafel form) to eq 6, showing the dependence of α on scan rate.

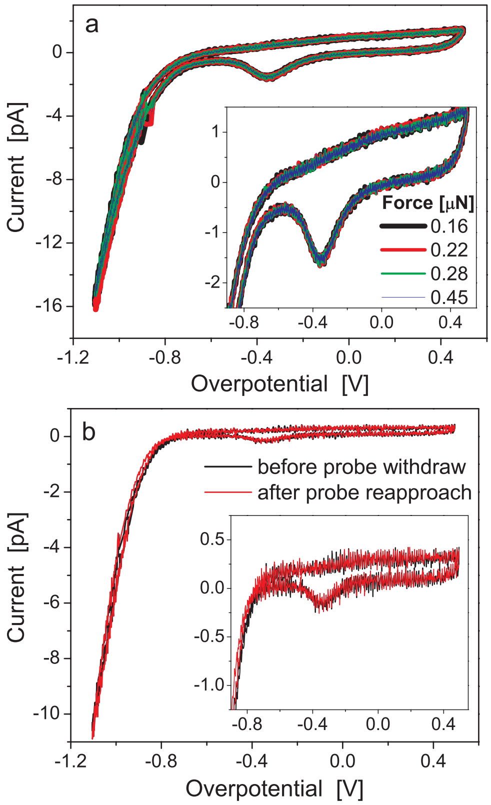

Figure 13. Cyclic voltammograms for Pt|$CsHSO_4$ collected at ∼150 °C in humidified air with ∼0.01−0.03 atm H_2O (a) at forces, ranging from 0.16 to 0.45 μN, applied between the probe and the $CsHSO_4$ surface (probe 6) and (b) at the same location on the surface, before withdrawing the probe and after reapproaching (probe 3).

Acknowledgment. Funding for this project was provided by the Gordon and Betty Moore Foundation through the Caltech Center for Sustainable Energy Research and by the National Science Foundation through the Caltech Center for the Science and Engineering of Materials, a Materials Research Science and Engineering Center (DMR-052056). M.W.L. was supported in part through the NSF Graduate Research Fellowship Program. The authors thank Brian Sayers at Solartron Analytical and Dr. Shijie Wu at Agilent Technologies for assistance with instrumentation.

REFERENCES AND NOTES

1. la O', G. J.; Shao-Horn, Y. Oxygen Surface Exchange Kinetics on Sr-Substituted Lanthanum Manganite and Ferrite Thin-Film Microelectrodes. *J. Electrochem. Soc.* **2009**, *156*, B816–B824.
2. Baumann, F. S.; Fleig, J.; Habermeier, H. U.; Maier, J. Impedance Spectroscopic Study on Well-Defined (La, Sr)(Co, Fe)$O_{3-\delta}$ Model Electrodes. *Solid State Ionics* **2006**, *177*, 1071–1081.
3. Fleig, J. Microelectrodes in Solid State Ionics. *Solid State Ionics* **2003**, *161*, 279–289.
4. O'Hayre, R.; Prinz, F. B. The Air/Platinum/Nafion Triple-Phase Boundary: Characteristics, Scaling, and Implications for Fuel Cells. *J. Electrochem. Soc.* **2004**, *151*, A756–A762.
5. Chueh, W. C.; Haile, S. M. Electrochemical Studies of Capacitance in Cerium Oxide Thin Films and Its Relationship to Anionic and Electronic Defect Densities. *Phys. Chem. Chem. Phys.* **2009**, *11*, 8144–8148.
6. Hertz, J. L.; Tuller, H. L. Electrochemical Characterization of Thin Films for a Micro-Solid Oxide Fuel Cell. *J. Electroceram.* **2004**, *13*, 663–668.
7. Louie, M. W.; Sasaki, K.; Haile, S. M. Towards Understanding Electrocatalysis in CsH_2PO_4-Based Fuel Cells: Platinum and Palladium Thin Film Electrodes. *ECS Trans.* **2008**, *13*, 57–62.
8. Jung, W.; Tuller, H. L. Investigation of Cathode Behavior of Model Thin-Film $SrTi_{1-x}Fe_xO_{3-\delta}$ ($x = 0.35$ and 0.5) Mixed Ionic-Electronic Conducting Electrodes. *J. Electrochem. Soc.* **2008**, *155*, B1194–B1201.
9. Bieberle, A.; Meier, L. P.; Gauckler, L. J. The Electrochemistry of Ni Pattern Anodes Used as Solid Oxide Fuel Cell Model Electrodes. *J. Electrochem. Soc.* **2001**, *148*, A646–A656.
10. Mizusaki, J.; Tagawa, H.; Saito, T.; Yamamura, T.; Kamitani, K.; Hirano, K.; Ehara, S.; Takagi, T.; Hikita, T.; Ippommatsu, M.; *et al.* Kinetic Studies of the Reaction at the Nickel Pattern Electrode on YSZ in H_2-H_2O Atmospheres. *Solid State Ionics* **1994**, *70−71*, 52–58.
11. Radhakrishnan, R.; Virkar, A. V.; Singhal, S. C. Estimation of Charge-Transfer Resistivity of $La_{0.8}Sr_{0.2}MnO_3$ Cathode on $Y_{0.16}Zr_{0.84}O_2$ Electrolyte Using Patterned Electrodes. *J. Electrochem. Soc.* **2005**, *152*, A210–A218.
12. Sasaki, K. A.; Hao, Y.; Haile, S. M. Geometrically Asymmetric Electrodes for Probing Electrochemical Reaction Kinetics: A Case Study of Hydrogen at the $Pt-CsH_2PO_4$ Interface. *Phys. Chem. Chem. Phys.* **2009**, *11*, 8349–8357.
13. Schmidt, M. S.; Hansen, K. V.; Norrman, K.; Mogensen, M. Effects of Trace Elements at the Ni/ScYSZ Interface in a Model Solid Oxide Fuel Cell Anode. *Solid State Ionics* **2008**, *179*, 1436–1441.
14. Atkinson, A.; Barnett, S.; Gorte, R. J.; Irvine, J. T. S.; McEvoy, A. J.; Mogensen, M.; Singhal, S. C.; Vohs, J. Advanced Anodes for High-Temperature Fuel Cells. *Nature* **2004**, *3*, 17–27.
15. Jiang, S. P.; Chan, S. H. A Review of Anode Materials Development in Solid Oxide Fuel Cells. *J. Mater. Sci.* **2004**, *39*, 4405–4439.
16. Adler, S. B. Factors Governing Oxygen Reduction in Solid Oxide Fuel Cell Cathodes. *Chem. Rev.* **2004**, *104*, 4791–4843.
17. Litster, S.; McLean, G. PEM Fuel Cell Electrodes. *J. Power Sources* **2004**, *130*, 61–76.
18. O'Hayre, R.; Lee, M.; Prinz, F. B. Ionic and Electronic Impedance Imaging Using Atomic Force Microscopy. *J. Appl. Phys.* **2004**, *95*, 8382–8392.
19. Bussian, D. A.; O'Dea, J. R.; Metiu, H.; Buratto, S. K. Nanoscale Current Imaging of the Conducting Channels in Proton Exchange Membrane Fuel Cells. *Nano Lett.* **2007**, *7*, 227–232.
20. Aleksandrova, E.; Hiesgen, R.; Friedrich, K. A.; Roduner, E. Electrochemical Atomic Force Microscopy Study of Proton Conductivity in a Nafion Membrane. *Phys. Chem. Chem. Phys.* **2007**, *9*, 2735–2743.
21. Takimoto, N.; Ohira, A.; Takeoka, Y.; Rikukawa, M. Surface Morphology and Proton Conduction Imaging of Nafion Membrane. *Chem. Lett.* **2008**, *37*, 164–165.
22. Layson, A.; Gadad, S.; Teeters, D. Resistance Measurements at the Nanoscale: Scanning Probe AC Impedance Spectroscopy. *Electrochim. Acta* **2003**, *48*, 2207–2213.
23. Vels Hansen, K.; Jacobsen, T.; Norgaard, A.-M.; Ohmer, N.; Mogensen, M. Scanning Probe Microscopy at 650 °C in Air. *Electrochem. Solid-State Lett.* **2009**, *12*, B144–B145.
24. Loster, M.; Friedrich, K. A.; Scherson, D. A. Assembly and Electrochemical Characterization of Nanometer-Scale Electrode|Solid Electrolyte Interfaces. *J. Phys. Chem. B* **2006**, *110*, 18081–18087.
25. O'Hayre, R.; Feng, G.; Nix, W. D.; Prinz, F. B. Quantitative Impedance Measurement Using Atomic Force Microscopy. *J. Appl. Phys.* **2004**, *96*, 3540–3549.
26. Baranov, A. I.; Shuvalov, L. A.; Shchagina, N. M. Superion Conductivity and Phase Transitions in $CsHSO_4$ and $CsHSeO_4$ Crystals. *JETP Lett.* **1982**, *36*, 459–462.
27. Norby, T.; Friesel, M.; Mellander, B. E. Proton and Deuteron Conductivity in $CsHSO_4$ and $CsDSO_4$ by *In Situ* Isotopic Exchange. *Solid State Ionics* **1995**, *77*, 105–110.
28. Haile, S. M.; Boysen, D. A.; Chisholm, C. R. I.; Merle, R. B. Solid Acids as Fuel Cell Electrolytes. *Nature* **2001**, *410*, 910–913.
29. Boysen, D. A.; Uda, T.; Chisholm, C. R. I.; Haile, S. M. High-Performance Solid Acid Fuel Cells through Humidity Stabilization. *Science* **2004**, *303*, 68–70.
30. Haile, S. M.; Chisholm, C. R. I.; Sasaki, K.; Boysen, D. A.; Uda, T. Solid Acid Proton Conductors: From Laboratory Curiosities to Fuel Cell Electrolytes. *Faraday Discuss.* **2007**, *134*, 17–39.
31. Adler, S. B. Reference Electrode Placement in Thin Solid Electrolytes. *J. Electrochem. Soc.* **2002**, *149*, E166–E172.
32. Rutman, J.; Riess, I. Placement of Reference Electrode in Solid Electrolyte Cells. *Electrochim. Acta* **2007**, *52*, 6073–6083.
33. *HSC Chemistry 5.0*; Outokumpu Research Oy, copyright 1974−2002.
34. Birss, V. I.; Chang, M.; Segal, J. Platinum Oxide Film Formation-Reduction: An *In-Situ* Mass Measurement Study. *J. Electroanal. Chem.* **1993**, *355*, 181–191.
35. Hsueh, K.-L.; Gonzalez, E. R.; Srinivasan, S. Effects of Phosphoric Acid Concentration on Oxygen Reduction Kinetics at Platinum. *J. Electrochem. Soc.* **1984**, *131*, 823–828.
36. Tammeveski, K.; Tenno, T.; Claret, J.; Ferrater, C. Electrochemical Reduction of Oxygen on Thin-Film Pt Electrodes in 0.1 M KOH. *Electrochim. Acta* **1997**, *42*, 893–897.
37. Paik, C. H.; Jarvi, T. D.; O'Grady, W. E. Extent of PEMFC Cathode Surface Oxidation by Oxygen and Water Measured by CV. *Electrochem. Solid-State Lett.* **2004**, *7*, A82–A84.
38. Xu, H.; Kunz, R.; Fenton, J. M. Investigation of Platinum Oxidation in PEM Fuel Cells at Various Relative Humidities. *Electrochem. Solid-State Lett.* **2007**, *10*, B1–B5.
39. Bard, A. J.; Faulkner, L. R. *Electrochemical Methods: Fundamentals and Applications*, 2nd ed.; John Wiley & Sons: New York, 2001; pp 94−100.
40. Zhai, Y.; Zhang, H.; Xing, D.; Shao, Z.-G. The Stability of Pt/C Catalyst in H_3PO_4/PBI PEMFC During High Temperature Life Test. *J. Power Sources* **2007**, *164*, 126–133.
41. Song, Y.; Fenton, J. M.; Kunz, H. R.; Bonville, L. J.; Williams, M. V. High-Performance PEMFCs at Elevated Temperatures Using Nafion 112 Membranes. *J. Electrochem. Soc.* **2005**, *152*, A539–A544.

42. Kwon, K.; Park, J. O.; Yoo, D. Y.; Yi, J. S. Phosphoric Acid Distribution in the Membrane Electrode Assembly of High Temperature Proton Exchange Membrane Fuel Cells. *Electrochim. Acta* **2009**, *54*, 6570–6575.
43. Aragane, J.; Urushibata, H.; Murahashi, T. Evaluation of an Effective Platinum Metal Surface Area in a Phosphoric Acid Fuel Cell. *J. Electrochem. Soc.* **1994**, *141*, 1804–1808.
44. Jiang, S. P.; Love, J. G.; Badwal, S. P. S. Electrochemical Techniques in Studies of Solid Ionic Conductors. In *Electrical Properties of Oxide Materials*; Nowotny, J., Sorrell, C. C., Eds.; Trans Tech Publications: Zurich, Switzerland, 1997; Vols. *125−126*, pp 81−132.
45. Macdonald, J. R. *Impedance Spectroscopy*; John Wiley & Sons: New York, 1987; p 13.
46. Fouda-Onana, F.; Bah, S.; Savadogo, O. Palladium−Copper Alloys as Catalysts for the Oxygen Reduction Reaction in an Acidic Media I: Correlation between the ORR Kinetic Parameters and Intrinsic Physical Properties of the Alloys. *J. Electroanal. Chem.* **2009**, *636*, 1–9.
47. Kumar, S.; Zou, S. Electrooxidation of CO on Uniform Arrays of Au Nanoparticles: Effects of Particle Size and Interparticle Spacing. *Langmuir* **2009**, *25*, 574–581.
48. Murthi, V. S.; Urian, R. C.; Mukerjee, S. Oxygen Reduction Kinetics in Low and Medium Temperature Acid Environment: Correlation of Water Activation and Surface Properties in Supported Pt and Pt Alloy Electrocatalysts. *J. Phys. Chem. B* **2004**, *108*, 11011–11023.
49. Parthasarathy, A.; Srinivasan, S.; Appleby, A. J.; Martin, C. R. Temperature Dependence of the Electrode Kinetics of Oxygen Reduction at the Platinum/Nation Interface—A Microelectrode Investigation. *J. Electrochem. Soc.* **1992**, *139*, 2530–2537.
50. Remita, H.; Siril, P. F.; Mbomekalle, I.-M.; Keita, B.; Nadjo, L. Activity Evaluation of Carbon Paste Electrodes Loaded with Pt Nanoparticles Prepared in Different Radiolytic Conditions. *J. Solid State Electrochem.* **2006**, *10*, 506–511.
51. Takasu, Y.; Ohashi, N.; Zhang, X.-G.; Murakami, Y.; Minagawa, H.; Sato, S.; Yahikozawa, K. Size Effects of Platinum Particles on the Electroreduction of Oxygen. *Electrochim. Acta* **1996**, *41*, 2595–2600.
52. Tilak, B. V.; Chen, C.-P.; Birss, V. I.; Wang, J. Capacitive and Kinetic Characteristics of Ru−Ti Oxides Electrodes: Influence of Variation in the Ru Content. *Can. J. Chem.* **1997**, *75*, 1773–1782.
53. Uchida, H.; Yoshida, M.; Watanabe, M. Effects of Ionic Conductivities of Zirconia Electrolytes on Polarization Properties of Platinum Anodes in Solid Oxide Fuel Cells. *J. Phys. Chem.* **1995**, *99*, 3282–3287.